ADVANCED FUNCTIONAL MATERIALS
www.afm-journal.de

Predicting Mechanical and Thermal Properties of High-Entropy Ceramics via Transferable Machine-Learning-Potential-Based Molecular Dynamics

Yiwen Liu, Hong Meng, Zijie Zhu, Hulei Yu, Lei Zhuang, and Yanhui Chu**

The mechanical and thermal performance of high-entropy ceramics are critical to their use in extreme conditions. However, the vast composition space of high-entropy ceramics significantly hinders their development with desired mechanical and thermal properties. Herein, taking high-entropy carbides (HECs) as the model, the efficiency and effectiveness of predicting mechanical and thermal properties via transferable machine-learning-potential-based molecular dynamics (MD) have been demonstrated. Specifically, a transferable neuroevolution potential (NEP) with broad compositional applicability for HECs of ten transition metal elements from group IIIB-VIB is efficiently constructed from the small dataset comprising unary and binary carbides with an equal amount of ergodic chemical compositions. Based on this well-established transferable NEP, MD predictions on mechanical and thermal properties of different HECs have shown good agreement with the results of first-principles calculations and experimental measurements, validating the accuracy, transferability, and reliability of using the transferable machine-learning-potential-based MD simulations in investigating mechanical and thermal performance of HECs. This work provides a strategy to accelerate the search for high-entropy ceramics with desirable mechanical and thermal properties.

1. Introduction

High-entropy ceramics, a class of emergent multicomponent materials with four or more principal elements, have attracted substantial attention in the ceramic community since they were first proposed in 2015.[1–4] Owing to their compositional complexity and unique microstructures, high-entropy ceramics have been shown to possess a range of superior properties exceeding those of their individual component ceramics, such as better thermal stability,[1,2,5,6] enhanced mechanical properties,[3,4,7,8] exceptional oxidation and ablation resistance,[9–12] higher catalytic activity,[13,14] improved thermoelectricity,[15,16] and remarkable superionic conductivity.[17] These distinctive characteristics have made them great potential for various structural applications, such as hypersonic thermal protection systems and high-speed cutting tools, as well as functional applications, like catalysts, thermoelectrics, and electrodes.

The investigations of mechanical and thermal properties are essential for high-entropy ceramics' use as structural materials, especially in extreme circumstances. To date, various exceptional mechanical and thermal properties, like high hardness and modulus,[3,4,8] enhanced flexural strength,[18,19] improved high-temperature creep resistance,[20] and lowered thermal conductivity and coefficients of thermal expansion (CTEs),[5,6,21] have been reported in high-entropy ceramics. Nevertheless, research on mechanical and thermal properties of high-entropy ceramics is still in the early stages. Due to the large composition space, the traditional experimental approaches to searching for high-entropy ceramics with desirable mechanical and thermal characteristics are both time-consuming and costly, failing to meet the growing demand from future structural application domains. Hence, it is imperative to develop an efficient method to comprehensively predict the mechanical and thermal properties of high-entropy ceramics. To this end, molecular dynamics (MD) simulations based on machine learning potentials (MLPs), as a frontier data-driven approach, have emerged as an effective and powerful solution.[22–24] Although studies of MLPs in predicting material properties have been carried out in high-entropy alloys (HEAs) and ceramic systems,[25–27] like TiO_2,[28] Ti_3O_5,[29] and TiB_2,[30] the applications of MLPs in high-entropy ceramics are seldom reported, with only two attempts proposed by Dai et al. on constructing MLPs for $(Ti_{1/5}Zr_{1/5}Hf_{1/5}Nb_{1/5}Ta_{1/5})B_2$ and $(Zr_{1/5}Hf_{1/5}Ti_{1/5}Nb_{1/5}Ta_{1/5})C$.[31,32] The dominant constraint lies in the poor transferability of the trained MLP with the conventional construction strategy, where the MLP was trained from a fixed-composition dataset, greatly hindering the comprehensive predictions of mechanical and thermal properties in different materials. Recent studies have demonstrated improved transferability in MLPs trained with varied compositions in HEAs, promoting machine-learning-potential-based MD simulations on their plasticity and primary

---

Y. Liu, H. Meng, Z. Zhu, H. Yu, L. Zhuang, Y. Chu
School of Materials Science and Engineering
South China University of Technology
Guangzhou 510641, China
E-mail: huleiyu@scut.edu.cn; chuyh@scut.edu.cn

The ORCID identification number(s) for the author(s) of this article can be found under https://doi.org/10.1002/adfm.202418802

DOI: 10.1002/adfm.202418802

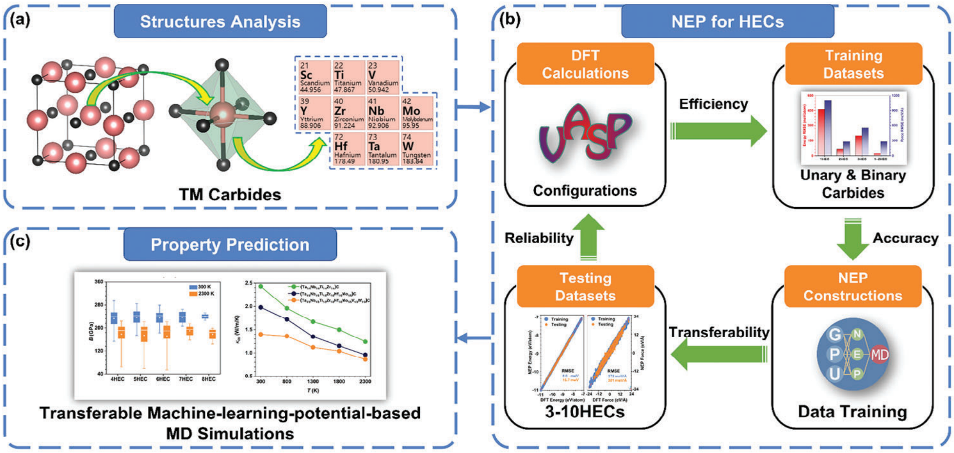

Figure 1. Schematic of transferable machine-learning-potential-based MD simulations for HECs. a) Crystal structure and the polyhedral of TM carbides with ten TM elements. TM and carbon atoms are colored in pink and black, respectively. b) Strategy to construct NEP for HECs. c) Transferable machine-learning-potential-based MD simulations on mechanical and thermal properties of HECs.

radiation damage performance.[33] However, there is still a lack of transferable MLPs with broad compositional applicability to enable the effective and economical exploitation of high-entropy ceramics with desired mechanical and thermal properties.

High-entropy carbides (HECs) are promising ultrahigh-temperature ceramics due to their potential tailorable and remarkable mechanical and thermal performance.[3,4,7,8] In this work, taking the HEC system as an example, we systematically explore mechanical and thermal properties of HECs through transferable machine-learning-potential-based MD simulations. To be specific, a transferable neuroevolution potential (NEP) with high accuracy and transferability based on unary (1HEC; the carbides with n types of transition metal (TM) elements are notated as nHECs) and binary (2HEC) carbide training data with up to ten non-magnetic TM elements of group IIIB, IVB, VB, and VIB (see **Figure** 1a) is efficiently built, enabling accurate and transferable machine-learning-potential-based MD simulations on mechanical and thermal properties of HECs. Figure 1b displays the process of the NEP construction strategy for HECs, where various effects, including the computational cost and modeling complexity of density functional theory (DFT) computations as well as accuracy and transferability of NEPs trained from different datasets, on the construction of NEPs are discussed, and a combination of 1HEC and 2HEC (1+2HEC) configurations with an equal amount of all possible chemical compositions is identified as the optimal training dataset choice. The transferability and accuracy of the established NEP are then assessed and verified by considering its applicability to HECs. Moreover, the accuracy, transferability, and reliability of MD simulations with the trained NEP on predicting mechanical and thermal properties of HECs are validated by comparing the results of first-principles calculations and experimental measurements (see Figure 1c). Our results show that the transferable machine-learning-potential-based MD simulations can efficiently accelerate the discovery of HECs with desired mechanical and thermal properties.

2. Results and Discussion

The construction of transferable MLPs for HECs is the prerequisite to enable transferable machine-learning-potential-based MD simulations. Unlike HEAs, where the metal principal elements are closely packed together, the metal elements in high-entropy ceramics are always separated by non-metal elements. As can be seen from Figure 1a, the first-nearest-neighbor atoms of TM atoms in carbides are all carbon atoms, forming an octahedron with TM—C bonding. When it comes to HEC systems (see **Figure** 2a), such a simple atomic environment can also be perpetuated. Though there exists tiny local lattice distortion in specific atomic pair distance, the overall radial pair distribution function presented in Figure 2b still confirms the similarity of the atomic environment for both TM carbides and HECs, which is beneficial to the construction of MLP descriptors for different HECs.[23] This indicates the possible applicability of MLPs between training datasets of carbides and their solid solutions. Based on these findings, it is anticipated that transferable MLPs applicable to various nHECs can be efficiently yielded from the training datasets comprising configurations of limited types of nHECs.

To verify this hypothesis, the cost of building datasets and the performance of trained NEPs from different datasets were first investigated. In HECs, the number of TM elements has a significant influence on geometric modeling, resulting in different efficiencies in DFT calculations for each composition. As shown in Figure 2c, it is found that the elapsed times show an overall increasing trend from 1HECs to 10HECs, indicating an unfavorable efficiency in building training datasets with more TM elements in HECs. Such computational inefficiency can also be explained by the relatively lower symmetry in HECs with more TM elements. As 1–3HEC configurations have the highest computational speeds, NEPs were first trained based on small-scale training datasets of 1HEC, 2HEC, and 3HEC, respectively, and their performances are presented in Figures S1–S3 (Supporting Information) and Figure 2d. While the trained NEPs all possess high training accuracy with comparable root mean square

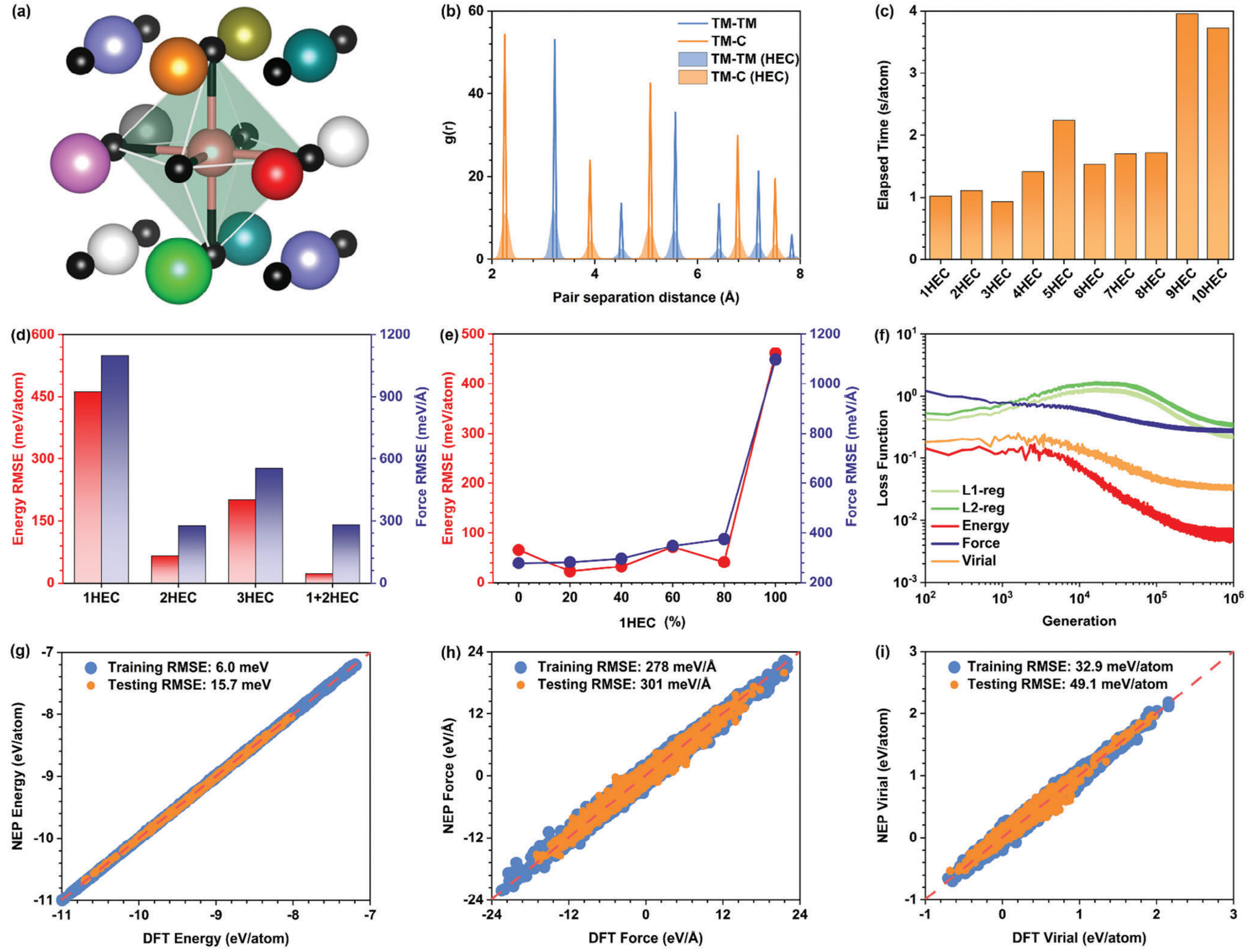

Figure 2. Construction and performance of NEP for HECs. a) Local crystal structure and polyhedral of HECs. Black atoms represent the carbon element, and other colored atoms represent different TM elements. b) Radial pair distribution function of TM carbides and HECs with the same lattice constants. c) Average elapsed time of *n*HECs in DFT calculations. d) Performance of NEPs with different training datasets (small-scale) to 1–10HEC testing datasets. e) Performance of NEPs with different 1+2HEC training datasets to 1–10HEC testing datasets. f) Evolution of various loss functions with respect to generations for the constructed NEP from the 1+2HEC training dataset (large-scale). g) Energy, h) force, and i) virial from NEP and DFT calculations for the 1+2HEC training dataset (large-scale) and the 3–10HEC testing dataset.

errors (RMSE) in energy (3.7–4.3 meV atom^{-1}), force (245–273 meV Å^{-1}), and virial (28.2-34.6 meV atom^{-1}), their transferability to the 1–10HEC testing dataset is quite different. Among the three trained NEPs, the one trained from the 1HEC training dataset performed the worst, showing low transferability in 1–10HEC systems. In contrast, the NEP from the 2HEC training dataset has better testing accuracy with significantly lower RMSEs of energy (65.6 meV atom^{-1}) and force (278 meV Å^{-1}), which indicates the enhanced transferability for *n*HEC systems and verifies our hypothesis. Furthermore, it is notable from Figure 2e and Figure S4–S7 (Supporting Information) that NEPs trained from the mixed 1+2HEC training datasets demonstrate better accuracy and transferability than NEPs from 1HEC and 2HEC training datasets, possessing much lower RMSEs of energy with a reduction of up to 65.7% besides the comparable RMSE of force. The best ratio of 1HEC: (1HEC+2HEC) is identified to be 18.18%, where equal numbers for all chemical compositions of 1HECs and 2HECs were used in training. In addition, ten TM elements can yield a total of 1023 equimolar compositions in 1–10HECs. For the 1+2HEC dataset, merely ten kinds of 1HECs and 45 kinds of 2HECs need to be taken into consideration, significantly simplifying the modeling processes for ab initio molecular dynamics (AIMD) calculations. Therefore, the 1+2HEC dataset with an equal amount of all possible chemical compositions is determined to be the most efficient training dataset.

The accuracy of the trained NEP can be further improved by increasing the volume of the training dataset.[24] Here, a larger 1+2HEC training dataset, configurations increasing from 1000 to 5500, was built to construct the NEP with high accuracy. As shown in Figure 2f, the L1 and L2 regularization loss functions show an increasing-then-decreasing trend over one million generations, indicating the effectiveness of the regularization. The loss of energy, force, and virial also converged, suggesting the

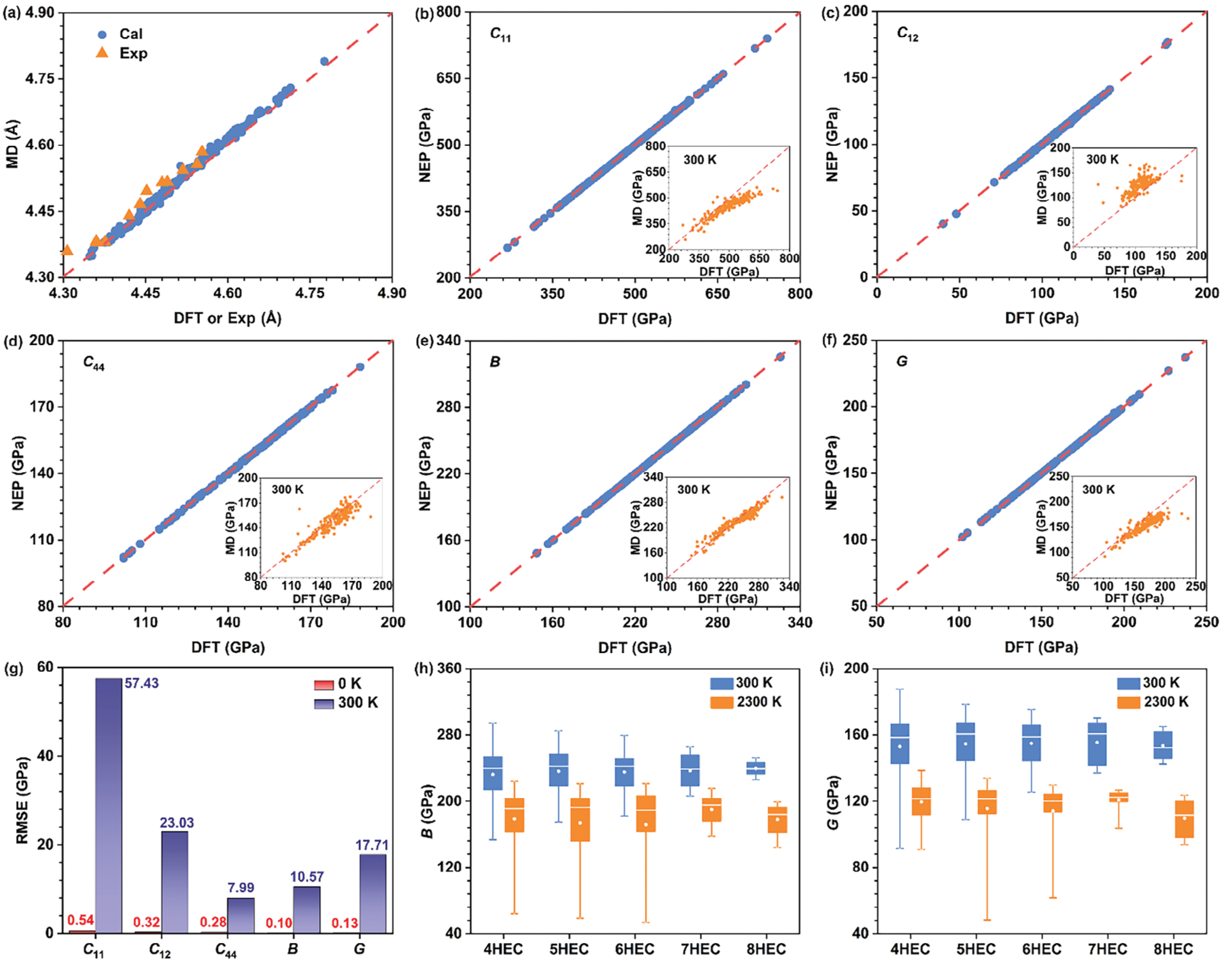

Figure 3. Comparison of structural and elastic properties of 4–8 HECs between machine-learning-potential-based MD simulations and DFT calculations. a) Lattice constants. Experimental data are from Ref.[6,34–37] Elastic tensors b) C_{11}, c) C_{12}, d) C_{44}, e) *B*, and f) *G* from NEP calculations with SQS models at 0 K compared with DFT calculations of SQS models at 0 K. The inserts show the consideration of size and temperature effects in machine-learning-potential-based MD simulations at 300 K. g) RMSEs for the above five quantities. h) *B* of 4–8HECs at 300 K and 2300 K. i) *G* of 4–8HECs at 300 K and 2300 K.

well-trained NEP. In addition, the increase in the volume of the 1+2HEC training dataset has no significant influence on their training accuracy (see Figure 2g–i). To examine the transferability of the trained NEP, a testing dataset based on 1500 kinds of 3–10HECs was built. It is notable that the enlarged volume of the training dataset can greatly improve the testing accuracy, achieving low testing RMSEs of 15.7 meV, 301 meV Å^{-1}, and 49.1 meV atom^{-1} in energy, force, and virial, respectively. Although the accuracy of the trained NEP is promising to be optimized further by introducing more training data (tens of thousands for most previous MLP works),[28,32] the present testing accuracies have already been sufficiently high for physical and chemical property explorations compared to previously reported MLPs,[29,31–33] demonstrating the remarkable efficiency, transferability, and accuracy of our established NEP for HECs. Moreover, only a minor fluctuation in testing accuracies can be observed in individual testing accuracies of *n*HEC (*n* = 3–10) testing datasets from Figure S8 (Supporting Information), indicating the transferability of our trained NEP to different HEC systems.

With the established transferable NEP, machine-learning-potential-based MD simulations can efficiently predict the mechanical and thermal performance of HECs. A total of 200 compositions of different 4–8HECs were randomly selected. As displayed in **Figure 3a**, the predicted lattice parameters (*a*) of 4–8HECs from machine-learning-potential-based MD simulations with our transferable NEP at 300 K are well consistent with DFT results and reported experiments,[6,34–37] indicating the reliability of our trained NEP. From Figure 3b–f, it can be found that the three elastic constants (C_{11}, C_{12}, and C_{44}) of HECs and the corresponding bulk modulus (*B*) and shear modulus (*G*) based on these constants predicted by machine-learning-potential-based MD simulations without size and temperature effects (using the energy-strain approach with the same special quasi-random structure (SQS) models at 0 K) exhibit remarkable alignment to those of DFT computations with the negligible value difference (see RMSEs in Figure 3g and the adjusted R-square (R^2_{adj}) in Figure S9, Supporting Information), showing the accuracy of machine-learning-potential-based MD predictions. On the contrary, large discrepancies can be observed between temperature-dependent MD results (64 000 atoms, 300 K) and DFT calculations (SQS models, 0 K) in Figure 3b–f, especially for C_{11}, C_{12}, and G (see large RMSEs in Figure 3g and low R^2_{adj} in Figure S9, Supporting Information). Such large disparities demonstrate the importance of the size effects (more disordered model) and temperature effects on the evaluations of the elastic properties of HECs,[30] thereby implying the necessity of using machine-learning-potential-based MD for HEC property predictions under temperature. Moreover, the elastic properties of different nHECs (n = 4–8) at both high temperature and low temperature were also explored. As shown in Figure 3h,i, it can be seen that the differences in the average B and G are tiny for 4–8HECs, and HECs with fewer TM elements tend to show larger value ranges at both low and high temperatures. Furthermore, the increase in temperature is determined to be detrimental to B and G for HECs, with an obvious overall decrease from 300 K to 2300 K. In addition, HECs with Sc and Y elements (i.e., ScY-based HECs) tend to have both lower B and G, whereas TaVW-based HECs and TiTa-based HECs are preferable to achieve higher B and G, respectively (see Figures S10, S11 and Tables S1, S2, Supporting Information). Notably, $(\mathrm{Nb}_{1/4}\mathrm{Ta}_{1/4}\mathrm{V}_{1/4}\mathrm{W}_{1/4})\mathrm{C}$ is found to possess the maximum B simultaneously at low temperature and high temperature among the predicted 200 HECs, while $(\mathrm{Ti}_{/4}\mathrm{Ta}_{1/4}\mathrm{V}_{1/4}\mathrm{W}_{1/4})\mathrm{C}$ and $(\mathrm{Ti}_{1/4}\mathrm{Nb}_{1/4}\mathrm{Ta}_{1/4}\mathrm{Hf}_{1/4})\mathrm{C}$ possess the largest G at 300 K and 2300 K, respectively. As a result, conclusions can be drawn that the established NEP has high accuracy and transferability in machine-learning-potential-based MD simulations for HECs.

Besides the structural and elastic properties, the applicability of machine-learning-potential-based MD simulations with our established NEP on the tensile strengths of 4HEC was also investigated. Taking the common 4HEC, $(\mathrm{Ta}_{1/4}\mathrm{Nb}_{1/4}\mathrm{Ti}_{1/4}\mathrm{Zr}_{1/4})\mathrm{C}$, as an example,[38] **Figure 4** presents the simulated tensile-testing results at 300 K. As depicted in Figure 4a–c, the ultimate tensile strengths of $(\mathrm{Ta}_{1/4}\mathrm{Nb}_{1/4}\mathrm{Ti}_{1/4}\mathrm{Zr}_{1/4})\mathrm{C}$ from machine-learning-potential-based MD simulations, which are the global stress maximum during the tensile tests,[30] are approximately 25.15, 37.00, and 35.41 GPa, for the [100], [110], and [111] directions, respectively, which is in agreement with the ones from AIMD values (22.97, 38.34, and 34.55 GPa, respectively). Notably, the slight discrepancies in results at high strains may be attributed to the underfitting of the datasets without fractured configurations. Meanwhile, the tensile toughness was also evaluated from the area underneath stress-strain curves.[30] The machine-learning-potential-based MD results are 1.58, 3.06, and 2.87 GPa for the [100], [110], and [111] directions, respectively, which are also comparable to those of AIMD results (1.43, 3.08, and 2.88 GPa, respectively). In addition, the predicted tensile strength and toughness from nanoscale models vary a lot with large strains, indicating the great influence of size effects similar to elastic properties. Moreover, the fracture surfaces formed during different deformations from AIMD (see Figure 4d–f) are also aligned with the results of machine-learning-potential-based MD simulations (see Figure 4g–i for SQS models and Figure S12, Supporting Information for nanoscale models), which are all approximately perpendicular to loading directions. It is notable that tensile loading along [100] will yield a void first in the fracture process, and the [110] tensile loading opens a zigzag fracture surface. Such exceptional quantitative agreement of stress-strain properties between machine-learning-potential-based MD and AIMD simulations indicates the reliability of machine-learning-potential-based MD simulations with our transferable NEP.

To validate the reliability of machine-learning-potential-based MD simulations with our trained NEP in studying the thermal properties of HECs, predictions on thermal conductivities of three typical HECs with different TM numbers at 300 K were first carried out. It should be noted that the electronic contribution of the thermal conductivity (κ_{ele}) has a significant influence on the total thermal conductivity (κ_{tot}) of HECs (see Table S3, Supporting Information) due to the gapless band structure of carbides,[39] while the one obtained from our machine-learning-potential-based MD simulations is merely the lattice part (κ_{lat}). Figure S13 (Supporting Information) shows the running lattice thermal conductivity (κ_{lat}) as a function of correlation time, where well-converged averaged κ_{lat} can be obtained in the range between 1.0 ns and 2.0 ns, indicating the reliability of our homogeneous nonequilibrium molecular dynamics (HNEMD) simulations. Meanwhile, it is found that there exists a slight decrease from $(\mathrm{Ta}_{1/4}\mathrm{Nb}_{1/4}\mathrm{Ti}_{1/4}\mathrm{Zr}_{1/4})\mathrm{C}$ to $(\mathrm{Ta}_{1/6}\mathrm{Nb}_{1/6}\mathrm{Ti}_{1/6}\mathrm{Zr}_{1/6}\mathrm{Hf}_{1/6}\mathrm{Mo}_{1/6})\mathrm{C}$ and then to $(\mathrm{Ta}_{1/8}\mathrm{Nb}_{1/8}\mathrm{Ti}_{1/8}\mathrm{Zr}_{1/8}\mathrm{Hf}_{1/8}\mathrm{Mo}_{1/8}\mathrm{V}_{1/8}\mathrm{W}_{1/8})\mathrm{C}$. Such a decrease can be understood by the spectral thermal conductivity $\kappa_{\mathrm{lat}}(\omega)$ in **Figure 5a**, where phonon modes in the range of 0–3 THz contribute the most to κ_{lat} with a significantly reduced tendency, suggesting a higher anharmonic scattering rate of low-frequency phonons. Moreover, the simulated κ_{lat} are found to be in good agreement with the experimental measurements (see Figure 5b), demonstrating the accuracy and applicability of machine-learning-potential-based MD predictions with our trained NEP in studying the thermal conductivities of HECs. In addition, the changes of κ_{lat} under temperature were further explored. As displayed in Figure 5c, all three HECs possess a decreased κ_{lat} with the increase in temperature, whereas their tendency ($(\mathrm{Ta}_{1/4}\mathrm{Nb}_{1/4}\mathrm{Ti}_{1/4}\mathrm{Zr}_{1/4})\mathrm{C} > (\mathrm{Ta}_{1/6}\mathrm{Nb}_{1/6}\mathrm{Ti}_{1/6}\mathrm{Zr}_{1/6}\mathrm{Hf}_{1/6}\mathrm{Mo}_{1/6})\mathrm{C} > (\mathrm{Ta}_{1/8}\mathrm{Nb}_{1/8}\mathrm{Ti}_{1/8}\mathrm{Zr}_{1/8}\mathrm{Hf}_{1/8}\mathrm{Mo}_{1/8}\mathrm{V}_{1/8}\mathrm{W}_{1/8})\mathrm{C}$) remains unchanged at both low and high temperature. Further studies on the mass fluctuations and the strain field fluctuations of the three HECs were conducted to present some clues of decreased κ_{lat}. As shown in Table S4 (Supporting Information), the mass fluctuations are also monotonically decreased from $(\mathrm{Ta}_{1/4}\mathrm{Nb}_{1/4}\mathrm{Ti}_{1/4}\mathrm{Zr}_{1/4})\mathrm{C}$ to $(\mathrm{Ta}_{1/6}\mathrm{Nb}_{1/6}\mathrm{Ti}_{1/6}\mathrm{Zr}_{1/6}\mathrm{Hf}_{1/6}\mathrm{Mo}_{1/6})\mathrm{C}$, then to $(\mathrm{Ta}_{1/8}\mathrm{Nb}_{1/8}\mathrm{Ti}_{1/8}\mathrm{Zr}_{1/8}\mathrm{Hf}_{1/8}\mathrm{Mo}_{1/8}\mathrm{V}_{1/8}\mathrm{W}_{1/8})\mathrm{C}$, which is inconsistent with the previous conclusion of higher mass fluctuations corresponds to lower κ_{lat}. This may imply the minor influence of mass fluctuation on κ_{lat} in HECs. In contrast, increased tendencies can be clearly observed in both volumetric and shear strain fluctuations (see Figure 5d–g) at both 300 K and 2300 K, indicating the lowered κ_{lat} in HECs may mainly be attributed to the aggravation of strain fluctuations, i.e., lattice distortion.

Besides thermal conductivities, CTEs of HECs were further predicted by machine-learning-potential-based MD simulations. **Figure 6a** shows the calculated results and reported

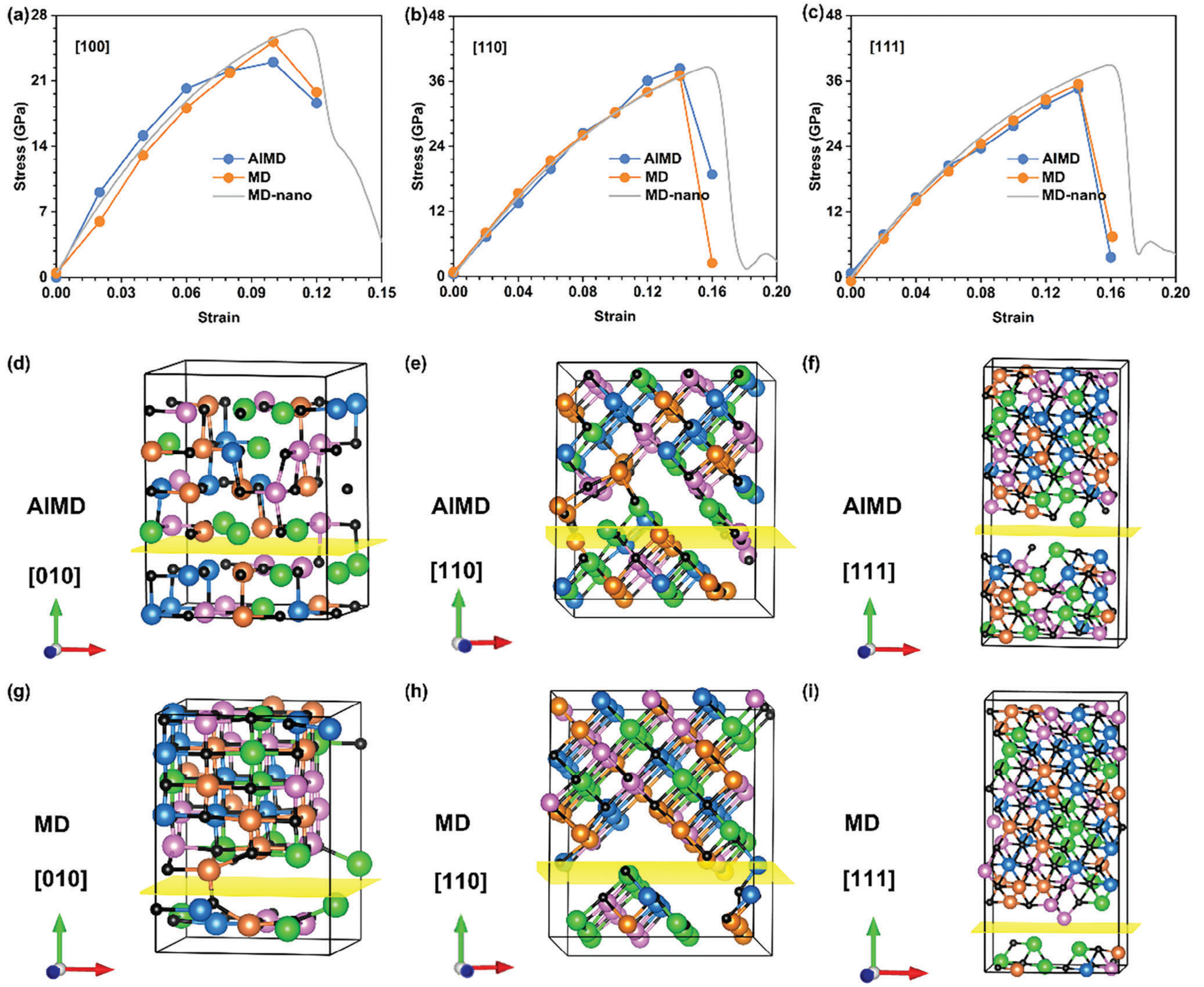

Figure 4. Tensile deformation for $(Ta_{1/4}Nb_{1/4}Ti_{1/4}Zr_{1/4})C$ with machine-learning-potential-based MD simulations and AIMD calculations. a–c) Stress-strain curves of SQS models and nanoscale models (MD-nano) at 300 K. d–f) Snapshots of fracture surfaces on (100), (110), and (111) planes from AIMD (0.12, 0.16, and 0.16 strain, respectively). g–i) Snapshots of fracture surfaces on (100), (110), and (111) planes from machine-learning-potential-based MD simulations (0.12, 0.16, and 0.16 strain, respectively). Black, orange, pink, blue, and green atoms represent the C, Ta, Nb, Ti, and Zr elements, respectively.

experimental values of different 1HECs.[40–48] The theoretical results are in good agreement with experimental reports (within the bounds of experimental measurements), verifying the reliability of our predictions. It should be mentioned that those 1HECs with large predicted CTEs, i.e., MoC, WC, YC, and ScC, are energetically unstable in their face-centered cubic (FCC) phases from a thermodynamic perspective.[39] Moreover, CTEs of the three above-mentioned typical HECs were also measured to enrich the limited available CTE data of HECs. As listed in **Table 1**, the calculated CTEs of HECs are comparable to the ones from our measurements and previous research with acceptable discrepancies,[32,45] further confirming the feasibility of our transferable machine-learning-potential-based MD predictions for HECs. In contrast, the rule of mixtures (ROM) method, generally regarded as an empirical way to roughly estimate the properties of HECs, was applied to evaluate CTEs of HECs in Table 1. A great disparity between the ROM method and those of experiments and reports can be found, which verifies the inaccuracy of the ROM method for HECs and shows the superiority of our MD predictions. From Figure 6b, it is clear to see that CTEs of 4–8HECs are all located within the predicted CTE bound of 1HECs (6.71-23.55 × 10^{-6} K^{-1}) at 300 K. It should be noted that, contrary to the high CTE predicted in the unstable MoC, VC, YC, and ScC, the relatively high CTE in $(Mo_{1/4}V_{1/4}Sc_{1/4}Y_{1/4})C$ at 300 K is attainable due to the promising phase formation ability (PFA) of $(Mo_{1/4}V_{1/4}Sc_{1/4}Y_{1/4})C$,[49] suggesting the feasibility of searching for exceptional performance in HECs with our transferable machine-learning-potential-based MD simulations. Meanwhile, it can also be found from Figure 6b that the ROM method has a tendency to overestimate the CTEs of HECs compared to our

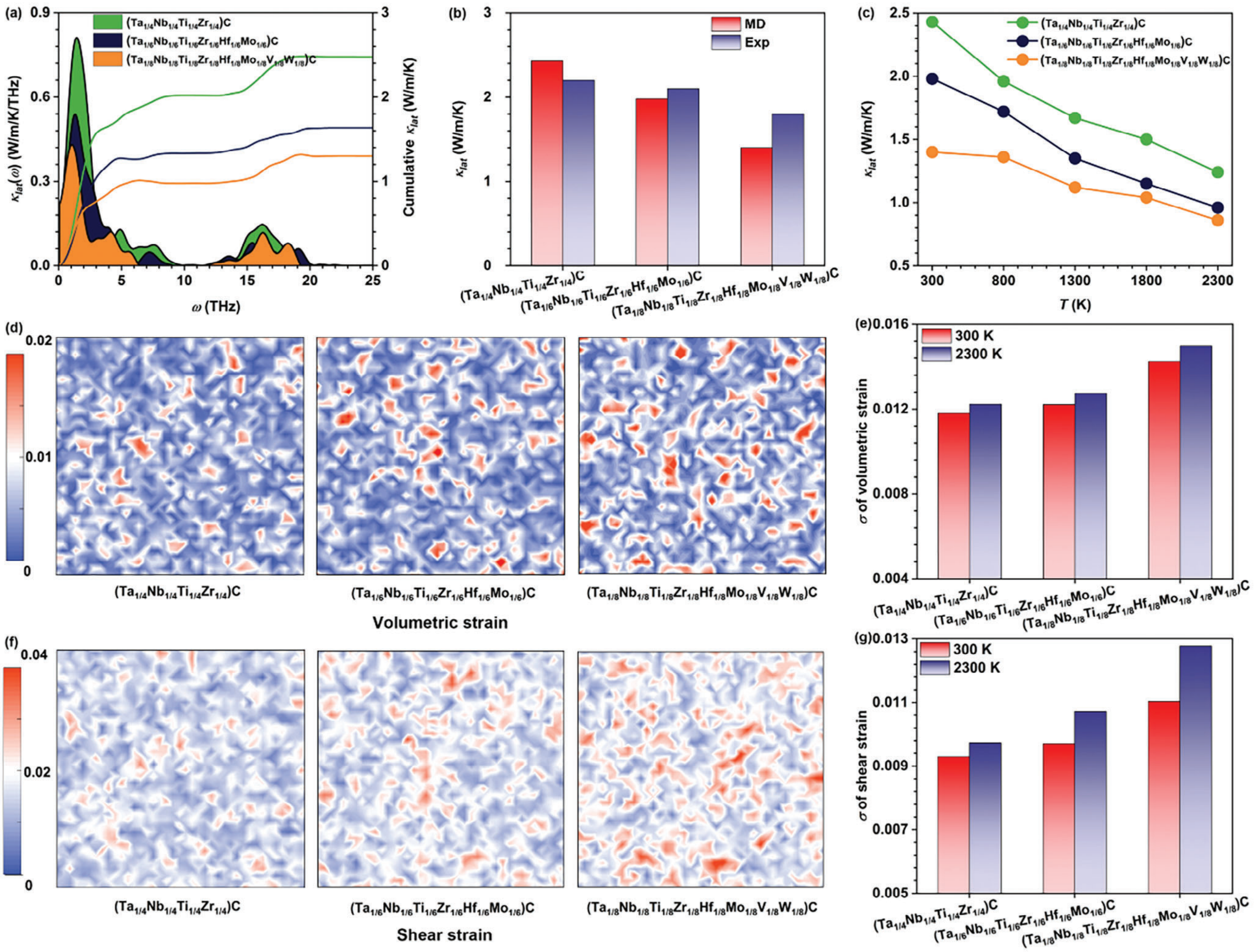

Figure 5. Thermal conductivities and strain field of $(Ta_{1/4}Nb_{1/4}Ti_{1/4}Zr_{1/4})C$, $(Ta_{1/6}Nb_{1/6}Ti_{1/6}Zr_{1/6}Hf_{1/6}Mo_{1/6})C$, and $(Ta_{1/8}Nb_{1/8}Ti_{1/8}Zr_{1/8}Hf_{1/8}Mo_{1/8}V_{1/8}W_{1/8})C$. a) $\kappa_{\mathrm{lat}}(\omega)$ and the cumulative κ_{lat}. b) Comparison of κ_{lat} between machine-learning-potential-based MD simulations and our measurements. c) Predicted κ_{lat} as a function of temperature. d) Volumetric strain distribution on a 2D slice of (100) plane. e) Standard deviations of volumetric strain at 300 K and 2300 K. f) Shear strain distribution on a 2D slice of (100) plane. g) Standard deviations of shear strain at 300 K and 2300 K.

predicted results. From Figure 6c, it can be deduced that HECs with fewer TM elements tend to possess larger or smaller CTEs, achieving the maxima values in $(Mo_{1/4}V_{1/4}Sc_{1/4}Y_{1/4})C$ at 300 K and $(Mo_{1/5}Ti_{1/5}V_{1/5}Sc_{1/5}Y_{1/5})C$ at 2300 K, and the minimum in $(Ti_{1/4}Zr_{1/4}Hf_{1/4}Ta_{1/4})C$ at 300 K and $(Ti_{1/4}Hf_{1/4}Ta_{1/4}Nb_{1/4})C$ at 2300 K (see Table S5, Supporting Information). Therefore, Ti, Hf, and Ta elements are preferable to lower the CTEs of HECs (see Figure S14, Supporting Information), which are beneficial to further applications of composites with silicon-based substrates. Additionally, the increase in temperature results in an obvious overall increase in CTEs from 300 K to 2300 K.

Since the melting points (T_m) of carbides are generally over 3200 K,[50–53] it is difficult to measure them directly in experiments. By utilizing transferable machine-learning-potential-based MD computations, the T_m of various HECs can be rapidly predicted. As shown in Figure 6d and Table S6 (Supporting Information), the theoretical predictions for T_m of 1HECs are all in good agreement with reported experiments (the average difference is less than 4.72%),[50–53] indicating the reliability of our transferable machine-learning-potential-based MD computations. From Figure 6e, it can be observed that the predicted T_m of HECs are all within the bound of predicted T_m of carbides, where W is determined to be preferable in enhancing T_m of HECs (see Figure S15, Supporting Information) and $(Ti_{1/4}Hf_{1/4}V_{1/4}W_{1/4})C$ has the largest T_m (4000 K) among all the predicted 4–8HECs (see Table S7, Supporting Information). In contrast, ZrY-based HECs tend to have lower T_m, reaching the lowest T_m of 2500 K in $(Zr_{1/4}V_{1/4}Sc_{1/4}Y_{1/4})C$ (see Table S7, Supporting Information). Although the T_m prediction of ROM in Figure 6e is improved compared to that in CTEs, it still tends to overestimate the values for 4–8HECs. Meanwhile, the T_m distribution of 4HECs is the widest (see Figure 6f), indicating the possibility of achieving higher T_m in HECs with fewer TM elements. Additionally, as previous studies have reported a potential correlation between the cohesive energy and CTEs or T_m,[54] the relationships between them in HECs

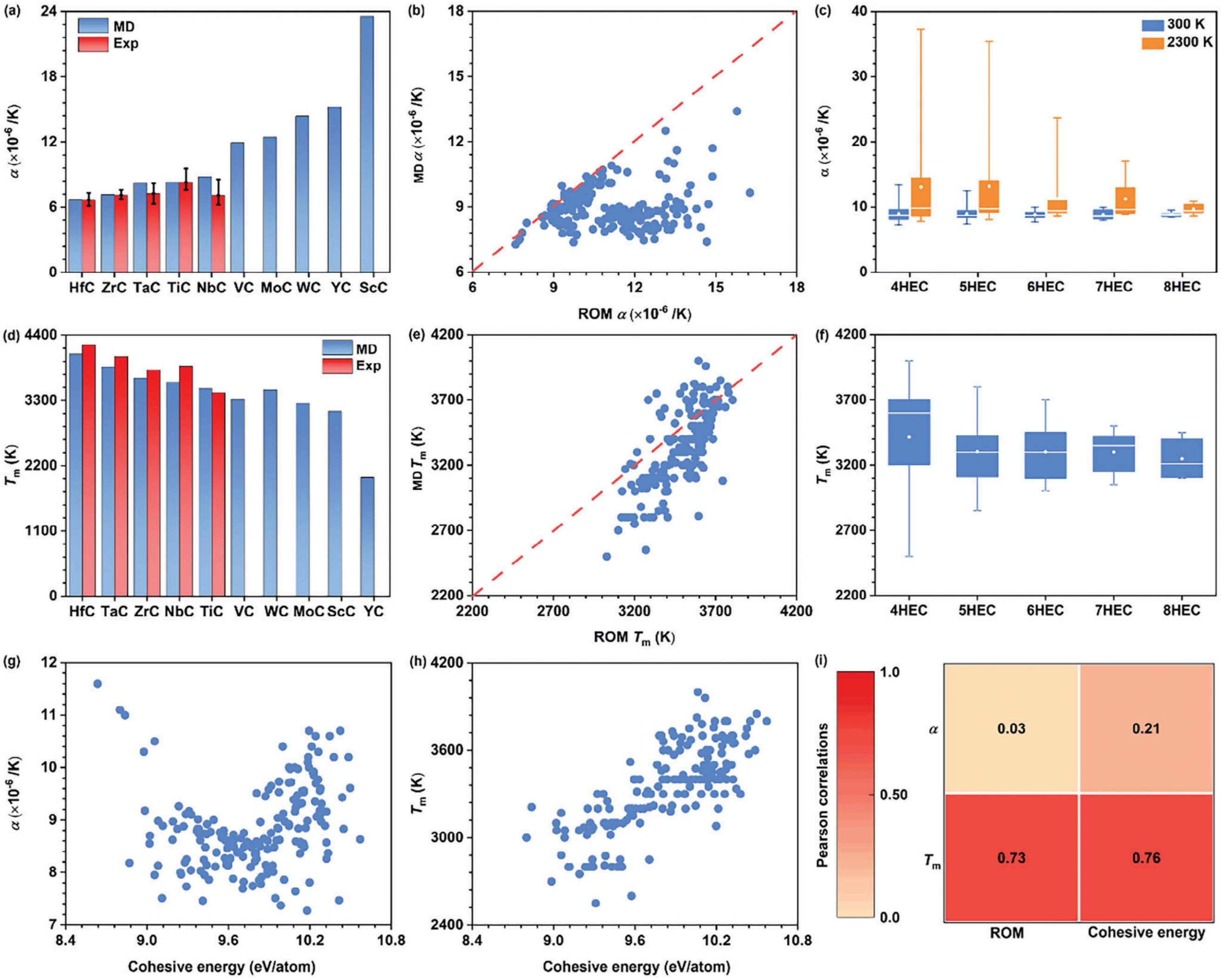

Figure 6. CTEs and T_m of *n*HECs from machine-learning-potential-based MD simulations with transferable NEP, reported experiments, and ROM calculations. a) CTEs of different 1HECs from machine-learning-potential-based MD simulations and reported experiments.[40–48] Error bars are the maximum and minimum of the reported values. b) CTEs of 4–8HECs between machine-learning-potential-based MD simulations and ROM calculations. c) CTEs of 4–8HECs at 300 K and 2300 K. d) T_m of different 1HECs from machine-learning-potential-based MD simulations and reported experiments.[50–53] e) T_m of different 4–8HECs between machine-learning-potential-based MD simulations and ROM calculations. f) T_m of 4–8HECs. g) Relationship between the cohesive energy and CTEs from machine-learning-potential-based MD simulations. h) Relationship between the cohesive energy and T_m from machine-learning-potential-based MD simulations. i) Pearson correlation between different properties.

were also explored. As shown in Figure 6g,h, it can be seen that CTEs have no evident correlation with the cohesive energy, while T_m is predicted to be strongly correlated to the cohesive energy. These results can also be obtained quantitatively by the Pearson correlation coefficients calculated in Figure 6i, where almost no correlations can be found for CTEs with ROM or cohesive energy, while the cohesive energy-T_m and ROM-T_m pairs are strongly correlated, unrevealing the importance of binding and elements of HECs on T_m.

3. Conclusion

In this work, we predicted the mechanical and thermal properties of HECs by enabling machine-learning-potential-based MD simulations via constructing a transferable NEP with wide compositional applicability for HECs. To be specific, the efficiency, accuracy, and transferability of the trained NEP for HECs based on the small 1+2HEC training dataset with an equal number of ergodic chemical compositions have been identified, resulting in the construction of a highly accurate and transferable NEP for HECs with low RSMEs of 15.7 meV atom^{-1}, 301 meV Å^{-1}, and 49.1 meV atom^{-1} for energy, force, and virial, respectively. On the basis of MD simulations with our established transferable NEP, mechanical and thermal properties, including elastic properties, tensile behaviors, κ_{lat}, CTEs, and T_m of HECs, are predicted to be consistent with results from first-principle calculations and experimental measurements, further validating the reliability of predicting mechanical and thermal properties of HECs with the transferable machine-learning-potential-based MD simulations. Our work provides a simple and efficient strategy for

Table 1. CTEs of HECs from transferable machine-learning-potential-based MD predictions, reported literature, our measurements, and ROM.

HECs	CTE [$\times 10^{-6}$/K]		
	Exp	MD	ROM
$(Ta_{1/4}Nb_{1/4}Ti_{1/4}Zr_{1/4})C$	7.05	8.00	8.59
$(Ti_{1/5}Zr_{1/5}Hf_{1/5}Ta_{1/5}W_{1/5})C$	7.70 (AIMD)[46]	8.05	9.29
$(Ti_{1/5}Zr_{1/5}Hf_{1/5}Nb_{1/5}Ta_{1/5})C$	7.85 (MD)[32]	7.82	8.28
$(Ta_{1/6}Nb_{1/6}Ti_{1/6}Zr_{1/6}Hf_{1/6}Mo_{1/6})C$	7.07	8.25	9.11
$(Ta_{1/8}Nb_{1/8}Ti_{1/8}Zr_{1/8}Hf_{1/8}Mo_{1/8}V_{1/8}W_{1/8})C$	7.06	8.84	10.20

developing high-entropy ceramics with desirable mechanical and thermal properties.

4. Experimental Section

DFT Calculations: All DFT calculations were implemented in the Vienna ab initio simulation package (VASP) with the projector augmented wave (PAW).[55,56] The Perdew-Burke-Ernzerhof (PBE) under the generalized gradient approximation (GGA) was applied to approximate the electronic exchange and correlation function.[57] Ten non-magnetic metallic elements of group IIIB, IVB, VB, and VIB were selected for ease of DFT calculations and DFT elapsed time comparison. Supercells of 1–10HECs were built based on the ZrC conventional cell, and the SQS approach was performed in the Alloy Theoretic Automated Toolkit (ATAT) for 2–10HECs.[58,59] Detailed supercell sizes are summarized in Table S8 (Supporting Information). All the structures were fully relaxed initially to obtain the lattice constants. Additionally, elastic tensors from DFT were calculated using the energy-strain approach.[60] Voigt-Reuss-Hill method was also used to evaluate the B and G of HECs.[61]

To build training and testing datasets, AIMD calculations with only the Γ point in the Brillouin zone considered were performed.[62] A low plane-wave energy cutoff of 300 eV was used to accelerate the collection of enough different structural configurations. A time step of 3 fs and a total simulation time of 6 ps were applied under the NPT ensemble. The simulated temperatures were set to 1000, 2000, 3000, and 4000 K, respectively. For high-accurate single-point calculations of configurations, the plane-wave cutoff energy was set to 450 eV, and the Brillouin zone was sampled employing the Γ-centered method with a separation of approximately 0.5 Å^{-1}.[63] The energy convergence criterion of the electronic self-consistency cycle was set to 10^{-5} eV.

For the AIMD simulations of the tensile deformation along different directions, SQS supercell models with 3×2×2 conventional cell of 96 atoms for the [100] direction, 2×2×3 [110] cell (x || [110], y || [$\bar{1}$10], z || [001]) of 192 atoms for the [110] direction, and 3×1×1 [111] cell (x || [111], y || [$\bar{1}2\bar{1}$], z || [$\bar{1}0\bar{1}$]) of 144 atoms for the [111] direction, respectively, were constructed. To ensure the accuracy and efficiency of the simulations, a time step of 1 fs and a cutoff energy of 400 eV was applied. Equilibration of all models at 300 K was first obtained for 1 ps relaxation under the NPT ensemble, followed by 1 ps NVT simulations, and then the equilibrated models were elongated along the corresponding direction with a 2% increment in strain. All the tensile supercells were then equilibrated under the NPT ensemble with the fixed directional elongation for 1 ps at each deformation step. The averaged stress tensors were collected for the final 0.1 ps.

NEP Constructions: Small-scale 1HEC, 2HEC, 3HEC, and 1+2HEC training datasets were first developed with each comprising 1000 configurations from AIMD calculations. The distribution of different TM elements in the datasets was ensured with the highest degree of equality. Different numbers of 1HEC configurations were considered in the small-scale 1+2HEC training datasets with ratios of 18.18% (equal numbers for all chemical compositions of 1HECs and 2HECs), 40%, 60%, and 80%. Based on these training datasets, state-of-the-art NEPs were then trained within the Graphics Processing Units Molecular Dynamics (GPUMD) code.[64] The detailed training hyperparameters are listed in Table S9 (Supporting Information). In addition, a corresponding testing dataset with 1–10HECs was constructed by a total of 300 randomly selected configurations (30 configurations for each nHEC) to evaluate the performance of the trained NEPs from these small-scale training datasets.

A large 1+2HEC training dataset containing 55 kinds of chemical compositions and 5500 configurations (100 configurations for each composition collected from AIMD) was built to train the accurate NEP for HECs. Meanwhile, 1500 configurations of randomly picked 71 kinds of HECs (ten kinds of chemical compositions each from 3–9HECs and the unique composition from 10HEC) were collected to build the 3–10HEC testing dataset with the best assurance of equally distributed TM elements. 20 configurations in each of the 3–9HEC compositions and 100 configurations in the 10HEC composition were selected from AIMD at the abovementioned four temperatures for static calculations.

Machine-Learning-Potential-Based Molecular Dynamics Simulations: The Large Scale Atomic/Molecular Massively Parallel Simulator (LAMMPS) package was utilized to perform MD simulations interfaced with the NEP code.[65] All the simulated models were built by randomizing the TM elements in a 20×20×20 FCC supercell (a total of 64 000 atoms). A time step of 1 fs was maintained throughout the simulations. Periodic boundary conditions were used in all directions. All models were first equilibrated using the NVT ensemble for a period of 10 ps, and then relaxed using the NPT ensemble for a period of 10 ps, and finally equilibrated using the NVT ensemble for a period of 10 ps at 300 K. Temperature-dependent elastic tensors were computed at 300 K and 2300 K, respectively, by taking Born term into account within 10 ps. The magnitude of strain was set to 10^{-6}. For a better comparison, elastic tensors of DFT SQS models using energy-strain methods were also evaluated with the NVT ensemble for 10 ps. The MD simulation setup of tensile deformation was performed at an engineering strain rate of 0.01 ps^{-1} for 20 ps. To consider the size effects, both the tensile deformations of the previous-mentioned SQS models and nanoscale models (20×20×20 conventional cell of 64 000 atoms for the [100] direction, 20×20×20 [110] cell of 128 000 atoms for the [110] direction, and 15×15×15 [111] cell 162 000 atoms for the [111] direction, respectively) were explored with the above-mentioned model equilibration. κ_{lat} was predicted by using the GPUMD package through the HNEMD method with a timestep of 1 fs and periodic boundary conditions.[64] All models were equilibrated for 20 ps using the NPT ensemble with a target temperature of 300 K before collecting the following 2 ns heat current data in the NVT ensemble. During HNEMD simulations, the driving force was chosen as $F_e = 0.0001$ Å^{-1}, and five independent simulations for each sample were performed to calculate the average thermal conductivity. A total correlation step of 200, a maximum angular frequency of 400 THz, and a sample interval of 2 were used for $\kappa_{\mathrm{lat}}(\omega)$ calculations. In addition, the mass fluctuations were computed as follows:

$$\text{Mass fluctuations} = \sum_i x_i \left(\frac{m_i - \bar{m}}{\bar{m}}\right)2 \tag{1}$$

where m_i is the atomic mass of the i-th element, x_i is the fractional concentration of the i-th element, and $\bar{m}$ is the average mass of all elements. The atomic strain tensor (ε^i_{ab}) was measured using the Green-Lagrangian strain tensor, and the volumetric strain and shear strain were defined as follows:[66]

$$\text{Volumetric strain} = \frac{\varepsilon^i_{xx} + \varepsilon^i_{yy} + \varepsilon^i_{zz}}{3} \tag{2}$$

$$\text{Shear strain} = \sqrt{{\varepsilon^i_{xy}}^2 + {\varepsilon^i_{xz}}^2 + {\varepsilon^i_{yz}}^2 + \frac{\left(\varepsilon^i_{xx} - \varepsilon^i_{yy}\right)^2 + \left(\varepsilon^i_{xx} - \varepsilon^i_{zz}\right)^2 + \left(\varepsilon^i_{yy} - \varepsilon^i_{zz}\right)^2}{6}} \tag{3}$$

Moreover, equilibrium lattice constants from 300 to 2300 K with an interval of 500 K were obtained, and the corresponding quadratic functions were fitted to evaluate CTEs at different temperatures. The T_m was simulated by first equilibrating at 2000 K for 100 ps using the NVT ensemble before being elevated to 4000 K with a heating rate of 5 K ps^{-1} using the NPT ensemble. The cohesive energy was computed by minimizing the potential energy of the HEC cells:

$$\text{Cohesive energy} = \sum_i E_i - E_{\text{HEC}} \tag{4}$$

where E_i and E_{HEC} are the potential energy of the i-th atom and the minimized HEC cell. The Pearson correlation between features and CTEs or T_m was evaluated to reveal the correlation between different properties:[67]

$$\text{Pearson correlation} = \frac{\sum (x_i - \bar{x})(y_i - \bar{y})}{\sqrt{\sum (x_i - \bar{x})^2 \sum (y_i - \bar{y})^2}} \tag{5}$$

where x_i and y_i are the i-th values of two different input features, respectively. $\bar{x}$ and $\bar{y}$ are the expectations of the two different input features, respectively.

Experimental Methods: The high-quality $(Ta_{1/4}Nb_{1/4}Ti_{1/4}Zr_{1/4})C$, $(Ta_{1/6}Nb_{1/6}Ti_{1/6}Zr_{1/6}Hf_{1/6}Mo_{1/6})C$, $(Ta_{1/8}Nb_{1/8}Ti_{1/8}Zr_{1/8}Hf_{1/8}Mo_{1/8}V_{1/8}W_{1/8})C$ samples were fabricated via a two-step strategy involving ultrafast high-temperature synthesis and hot-press sintering techniques. The detailed synthesis process can be found in this previous work.[38] The CTEs of the samples (13.5 mm × 3 mm × 3 mm) were measured over the temperature range of 373–998 K at a heating rate of 5 K min^{-1} in a nitrogen atmosphere by a high-temperature dilatometer (Netzsch DIL 402C, NETZSCH, Selb, Germany). The referenced temperature for calculating CTEs was 298 K. The thermal diffusivity (h) was measured at room temperature under an argon flow by a laser-flash apparatus (Netzsch LFA 427, Netzsch, Selb, Germany). κ_{tot} of the samples was evaluated according to the following equation:[68]

$$\kappa_{\text{tot}} = h \cdot \rho \cdot C_p \tag{6}$$

where C_p is the specific heat capacity estimated based on the Dulong-Petit law and ρ is the density of the samples measured by the Archimedes drainage method. As ρ of all samples were almost the same as theoretical ones, no correction on κ_{tot} was considered. In addition, the electrical conductivity (σ) of samples at room temperature was measured on a commercial apparatus (CTA-3, Cryoall, Beijing, China) under a helium atmosphere, and the corresponding κ_{ele} was computed according to Wiedemann-Franz law:[69]

$$\kappa_{\text{ele}} = L \cdot \sigma \cdot T \tag{7}$$

where $L = 2.44 \times 10^{-8}$ W Ω K^{-2} is the Lorenz number, and T is the absolute temperature. The lattice thermal conductivity ($\kappa_{\text{lat}} = \kappa_{\text{tot}} - \kappa_{\text{ele}}$) was thereby obtained.

Statistical Analysis: The statistical results in all boxplots were analyzed by Origin software and depicted as medians, means, maximums, and minimums. The Pearson correlation analysis was used with a prepared Python script.

Supporting Information

Supporting Information is available from the Wiley Online Library or from the author.

Acknowledgements

The authors acknowledge the financial support from the National Key Research and Development Program of China (No. 2021YFA0715801), the National Natural Science Foundation of China (No. 52122204 and 52402075), and the Guangzhou Basic and Applied Basic Research Foundation (SL2023A04J00690).

Conflict of Interest

The authors declare no conflict of interest.

Author Contributions

Y.C. conceived and designed this work. Y.L., H.M., and H.Y. performed calculations. Z.Z. and L.Z performed experiments. Y.C., H.Y, and Y.L analyzed the data and wrote the manuscript. All authors commented on the manuscript.

Data Availability Statement

The data that support the findings of this study are available from the corresponding author upon reasonable request.

Keywords

high-entropy ceramics, machine learning potentials, mechanical performance, molecular dynamics, thermal performance

Received: October 6, 2024
Revised: December 2, 2024
Published online: December 15, 2024

[1] C. Rost, E. Sachet, T. Borman, A. Moballegh, E. Dickey, D. Hou, J. Jones, S. Curtarolo, J. Maria, *Nat. Commun.* **2015**, *6*, 8485.
[2] J. Gild, Y. Zhang, T. Harrington, S. Jiang, T. Hu, M. C. Quinn, W. M. Mellor, N. Zhou, K. Vecchio, J. Luo, S. Rep, *Sci. Rep.* **2016**, *6*, 37946.
[3] B. Ye, T. Wen, K. Huang, C. Z. Wang, Y. Chu, *J. Am. Ceram. Soc.* **2019**, *102*, 4344.
[4] T. Wen, B. Ye, M. C. Nguyen, M. Ma, Y. Chu, *J. Am. Ceram. Soc.* **2020**, *103*, 6475.
[5] Z. Wen, Z. Tang, Y. Liu, L. Zhuang, H. Yu, Y. Chu, *Adv. Mater.* **2024**, *36*, 2311870.
[6] X. Yan, L. Constantin, Y. Lu, J. F. Silvain, M. Nastasi, B. Cui, *J. Am. Ceram. Soc.* **2018**, *101*, 4486.
[7] B. Ye, T. Wen, M. C. Nguyen, L. Hao, C. Z. Wang, Y. Chu, *Acta Mater.* **2019**, *170*, 15.
[8] M. Ma, Y. Han, Z. Zhao, J. Feng, Y. Chu, *J. Materiomics* **2023**, *9*, 370.
[9] Z. Tang, Z. Wen, Y. Liu, L. Zhuang, H. Yu, Y. Chu, *Adv. Funct. Mater.* **2024**, *34*, 2312239.
[10] Z. Wen, H. Meng, S. Jiang, Z. Tang, Y. Liu, Y. Chu, *Sci. China Mater* **2023**, *66*, 3213.
[11] Z. Wen, Z. Tang, H. Meng, Y. Chu, *Corros. Sci.* **2022**, *207*, 110574.
[12] Z. Wen, Z. Tang, H. Meng, L. Zhuang, H. Yu, Y. Chu, *Cell Rep. Phys. Sci.* **2024**, *5*, 101821.
[13] Y. Chu, R. Yu, G. He, T. Zhang, H. Dong, S. Deng, J. Li, *Sci. China Mater.* **2022**, *65*, 3144.
[14] R. Yu, Y. Liu, X. Sun, G. He, H. Dong, S. Deng, J. Li, Y. Chu, *Sci. China Mater* **2023**, *66*, 3582.
[15] P. Zhang, Z. Lou, G. Hu, Z. Wu, J. Xu, L. Gong, F. Gao, *J. Materiomics* **2023**, *9*, 661.
[16] A. Kumar, D. Dragoe, D. Berardan, N. Dragoe, *J. Materiomics* **2023**, *9*, 191.
[17] D. Bérardan, S. Franger, A. Meena, N. Dragoe, *J. Mater. Chem. A* **2016**, *4*, 9536.
[18] L. Feng, W. Fahrenholtz, G. Hilmas, Y. Zhou, J. Bai, *J. Am. Ceram. Soc.* **2023**, *107*, 1895.
[19] F. Wang, X. Zhang, X. Yan, Y. Lu, M. Nastasi, Y. Chen, B. Cui, *J. Am. Ceram. Soc.* **2020**, *103*, 4463.

[20] X. Han, V. Girman, R. Sedlak, J. Dusza, E. Castle, Y. Wang, M. Reece, C. Zhang, *J. Eur. Ceram. Soc.* **2020**, *7*, 2709.
[21] Y. Liu, L. Zhuang, P. Xie, H. Yu, Y. Chu, *Sci. China Mater* **2024**, *67*, 2694.
[22] Y. Mishin, *Acta Mater.* **2021**, *214*, 116980.
[23] J. Behler, *J. Chem. Phys.* **2016**, *145*, 170901.
[24] Y. Zuo, C. Chen, X. Li, Z. Deng, Y. Chen, J. Behler, G. Csányi, A. V. Shapeev, A. P. Thompson, M. A. Wood, S. P. Ong, *J. Phys. Chem. A* **2020**, *124*, 731.
[25] S. Chen, Z. Aitken, S. Pattamatta, Z. Wu, Z. Yu, D. Srolovitz, P. Liaw, Y. Zhang, *Nat. Commun.* **2021**, *12*, 4957.
[26] Y. F. Ye, Q. Wang, J. Lu, C. T. Liu, Y. Yang, *Mater. Today* **2016**, *19*, 349.
[27] W. Li, S. Lyu, Y. Chen, A. H. W. Ngan, *Proc. Natl. Acad. Sci. USA* **2023**, *120*, 2209188120.
[28] Z. Zeng, F. Wodaczek, K. Liu, F. Stein, J. Hutter, J. Chen, B. Cheng, *Nat. Commun.* **2023**, *14*, 6131.
[29] M. Liu, J. Wang, J. Hu, P. Liu, H. Niu, X. Yan, J. Li, H. Yan, B. Yang, Y. Sun, C. Chen, G. Kresse, L. Zuo, X. Q. Chen, *Nat. Commun.* **2024**, *15*, 3079.
[30] S. Lin, L. Casillas-Trujillo, F. Tasnádi, L. Hultman, P. H. Mayrhofer, D. G. Sangiovanni, N. Koutná, *npj Comput. Mater* **2024**, *10*, 67.
[31] F. Z. Dai, Y. Sun, B. Wen, H. Xiang, Y. Zhou, *J. Mater. Sci. Technol.* **2021**, *72*, 8.
[32] F. Z. Dai, B. Wen, Y. Sun, H. Xiang, Y. Zhou, *J. Mater. Sci. Technol.* **2020**, *43*, 168.
[33] K. Song, R. Zhao, J. Liu, Y. Wang, E. Lindgren, Y. Wang, S. Chen, K. Xu, T. Liang, P. Ying, *Nat. Commun.* **2024**, *15*, 10208.
[34] F. Wang, X. Yan, T. Wang, Y. Wu, L. Shao, M. Nastasi, Y. Lu, B. Cui, *Acta Mater.* **2020**, *195*, 739.
[35] J. Dusza, P. Švec, V. Girman, R. Sedlák, E. G. Castle, T. Csanádi, A. Kovalčíková, M. J. Reece, *J. Eur. Ceram. Soc.* **2018**, *38*, 4303.
[36] Z. Li, Z. Wang, Z. Wu, B. Xu, S. Zhao, W. Zhang, N. Lin, *Ceram. Int.* **2021**, *47*, 14341.
[37] K. Vasanthakumar, R. Gorle, S. Ariharan, S. R. Bakshi, *J. Eur. Ceram. Soc.* **2021**, *41*, 6756.
[38] Y. Liu, Z. Zhu, Z. Tang, H. Yu, L. Zhuang, Y. Chu, *Small* **2024**, *20*, 2403159.
[39] A. Jain, S. P. Ong, G. Hautier, W. Chen, W. D. Richards, S. Dacek, S. Cholia, D. Gunter, D. Skinner, G. Ceder, K. A. Persson, *APL Mater.* **2013**, *1*, 011002.
[40] Y. J. Wang, H. J. Li, Q. G. Fu, H. Wu, D. J. Yao, B. B. Wei, *Appl. Surf. Sci.* **2011**, *257*, 4760.
[41] B. Zhang, J. Yin, Y. Wang, D. Yu, H. Liu, X. Liu, M. J. Reece, Z. Huang, *J. Materiomics* **2021**, *7*, 672.
[42] Y. S. Touloukian, R. K. Kirby, E. R. M. Taylor, T. Y. R. Lee, vol. *13 Thermal Expansion-Nonmetallic Solids*, IFI/Plenum Data Company, New York, **1977**.
[43] J. H. Richardson, *J. Am. Ceram. Soc.* **1965**, *48*, 497.
[44] R. Riedel, *Handbook of Ceramic Hard Materials*, Wiley-VCH, Hoboken, New Jersey, USA **2000**.
[45] R. O. Elliott, C. P. Kempter, *J. Phys. Chem.* **1958**, *62*, 630.
[46] D. G. Sangiovanni, F. Tasnádi, T. Harrington, M. Odén, K. S. Vecchio, I. A. Abrikosov, *Mater. Des.* **2021**, *204*, 109634.
[47] B. A. Mathe, Surface Brillouin scattering studies of elastic properties of materials at high temperature, Univeristy of the Witwatersrand, Johannesburg, South Africa, **2008**.
[48] A. Krajewski, L. D'Alessio, G. De Maria, *Cryst. Res. Technol.* **1998**, *33*, 341.
[49] H. Meng, R. Yu, Z. Tang, Z. Wen, Y. Chu, *Cell Rep. Phys. Sci.* **2023**, *4*, 101512.
[50] O. Cedillos-Barraza, D. Manara, K. Boboridis, T. Watkins, S. Grasso, D. D. Jayaseelan, R. J. M. Konings, M. J. Reece, W. E. Lee, *Sci. Rep.* **2016**, *6*, 37962.
[51] D. L. Perry, *Handbook of inorganic compounds*, CRC Press, Boca Raton, Florida **2016**.
[52] M. G. D. V. Cuppari, S. F. Santos, *Metals* **2016**, *6*, 250.
[53] M. Bauccio, *ASM engineering materials reference book*, 2nd ed. ASM International, Metals Park, Ohio **1993**.
[54] V. L. Moruzzi, J. F. Janak, K. Schwarz, *Phys. Rev. B* **1988**, *37*, 790.
[55] G. Kresse, J. Furthmüller, *Comput. Mater. Sci.* **1996**, *6*, 15.
[56] P. E. Blöchl, *Phys. Rev. B* **1994**, *50*, 17953.
[57] J. P. Perdew, K. Burke, M. Ernzerhof, *Phys. Rev. Lett.* **1996**, *77*, 3865.
[58] A. Zunger, S. H. Wei, L. G. Ferreira, J. E. Bernard, *Phys. Rev. Lett.* **1990**, *65*, 353.
[59] A. van de Walle, *Calphad* **2009**, *33*, 266.
[60] V. Wang, N. Xu, J. C. Liu, G. Tang, W. T. Geng, *Comput. Phys. Commun.* **2021**, *267*, 108033.
[61] R. Hill, *Proc. Phys. Soc. A* **1952**, *65*, 349.
[62] R. Jinnouchi, J. Lahnsteiner, F. Karsai, G. Kresse, M. Bokdam, *Phys. Rev. Lett.* **2019**, *122*, 225701.
[63] H. J. Monkhorst, J. D. Pack, *Phys. Rev. B* **1976**, *13*, 5188.
[64] Z. Fan, Y. Wang, P. Ying, K. Song, J. Wang, Y. Wang, Z. Zeng, K. Xu, E. Lindgren, J. M. Rahm, A. J. Gabourie, J. Liu, H. Dong, J. Wu, Y. Chen, Z. Zhong, J. Sun, P. Erhart, Y. Su, T. Ala-Nissila, *J. Chem. Phys.* **2022**, *157*, 114801.
[65] A. P. Thompson, H. M. Aktulga, R. Berger, D. S. Bolintineanu, W. M. Brown, P. S. Crozier, P. J. in 't Veld, A. Kohlmeyer, S. G. Moore, T. D. Nguyen, R. Shan, M. J. Stevens, J. Tranchida, C. Trott, S. J. Plimpton, *Comput. Phys. Commun.* **2022**, *271*, 108171.
[66] A. Stukowski, *Modell. Simul. Mater. Sci. Eng.* **2009**, *18*, 015012.
[67] H. Meng, R. Yu, Z. Tang, Z. Wen, H. Yu, Y. Chu, *Acta Mater.* **2023**, *256*, 119132.
[68] M. C. Roufosse, P. G. Klemens, *Phys. Rev. B* **1973**, *7*, 5379.
[69] M. J. Graf, S. Yip, J. A. Sauls, D. Rainer, *Phys. Rev. B* **1996**, *53*, 15147.